LIMNOLOGY and OCEANOGRAPHY



Limnol. Oceanogr. 68, 2023, 1636–1653
© 2023 The Authors. Limnology and Oceanography published by Wiley Periodicals LLC on behalf of Association for the Sciences of Limnology and Oceanography.

Siderophore production and utilization by marine bacteria in the North Pacific Ocean

Jiwoon Park , ^{1*} Bryndan P. Durham , ² Rebecca S. Key, ² Ryan D. Groussman , ¹ Zinka Bartolek , ¹ Paulina Pinedo-Gonzalez , ³ Nicholas J. Hawco , ⁴ Seth G. John , ³ Michael C. G. Carlson , ⁵ Debbie Lindell , ⁵ Lauren W. Juranek , ⁶ Sara Ferrón , ⁴ François Ribalet , ¹ E. Virginia Armbrust , ¹ Anitra E. Ingalls , ¹ Randelle M. Bundy , ¹

Abstract

Siderophores are strong iron-binding molecules produced and utilized by microbes to acquire the limiting nutrient iron (Fe) from their surroundings. Despite their importance as a component of the iron-binding ligand pool in seawater, data on the distribution of siderophores and the microbes that use them are limited. Here, we measured the concentrations and types of dissolved siderophores during two cruises in April 2016 and June 2017 that transited from the iron-replete, low-macronutrient North Pacific Subtropical Gyre through the North Pacific Transition Zone (NPTZ) to the iron-deplete, high-macronutrient North Pacific Subarctic Frontal Zone (SAFZ). Surface siderophore concentrations in 2017 were higher in the NPTZ (4.0–13.9 pM) than the SAFZ (1.2–5.1 pM), which may be partly attributed to stimulated siderophore production by environmental factors such as dust-derived iron concentrations (up to 0.51 nM). Multiple types of siderophores were identified on both cruises, including ferrioxamines, amphibactins, and iron-free forms of photoreactive siderophores, which suggest active production and use of diverse siderophores across latitude and depth. Siderophore biosynthesis and uptake genes and transcripts were widespread across latitude, and higher abundances of these genes and transcripts at higher latitudes may reflect active siderophore-mediated iron uptake by the local bacterial community across the North Pacific. The variability in the taxonomic composition of bacterial communities that transcribe putative ferrioxamine, amphibactin, and salmochelin transporter genes at different latitudes further suggests that the microbial groups involved in active siderophore production and usage change depending on local conditions.

This is an open access article under the terms of the Creative Commons Attribution-NonCommercial-NoDerivs License, which permits use and distribution in any medium, provided the original work is properly cited, the use is non-commercial and no modifications or adaptations are made.

Additional Supporting Information may be found in the online version of this article.

Author Contribution Statement: JP analyzed siderophore samples and wrote the manuscript. JP and RMB designed the study. RMB collected siderophore field samples. RMB and AEI provided access, materials, and instrumentation for siderophore analysis. RDG, BPD, and EVA collected metatranscriptome field samples, RDG and ZB assembled the metatranscriptomes, and BPD and RSK analyzed the metatranscriptomes. MCGC and DL collected metagenome field samples and MCGC assembled the metagenomes. PPG, NJH, and SGJ collected and analyzed field samples for dissolved metals. LWJ collected and analyzed field samples for nutrients. FR collected and analyzed field samples for nutrients. FR collected and analyzed field samples for bacterial abundances. All authors edited and revised the manuscript.

Iron (Fe) is an essential nutrient for ocean life, but due to its low solubility in seawater, it often exists in concentrations far below the levels required for sustaining phytoplankton growth in over a third of open ocean surface waters (Johnson et al. 1997; Moore et al. 2013). More than 99% of the dissolved iron in the ocean is bound to organic ligands, as complexation of iron to organic ligands can increase the solubility of iron by orders of magnitude and prevent precipitation and scavenging (Gledhill and van den Berg 1994; Hunter and Boyd 2007; Gledhill and Buck 2012). In addition to increasing iron solubility, these organic ligands also affect the bioavailability of iron to phytoplankton and bacteria, playing a critical role in the ocean iron and other biogeochemical cycles (Hassler et al. 2012; Shaked et al. 2020).

Although the importance of iron-binding ligands to iron speciation and distributions in the ocean has been well recognized, the identity of these ligands, their sources and the

¹School of Oceanography, University of Washington, Seattle, Western Australia, USA

²Department of Biology, Genetics Institute, University of Florida, Gainesville, Florida, USA

³Department of Earth Sciences, University of Southern California, Los Angeles, California, USA

⁴Department of Oceanography, University of Hawai'i at Mānoa, Honolulu, Hawaii, USA

⁵Faculty of Biology, Technion Israel Institute of Technology, Haifa, Israel

⁶College of Earth, Ocean, and Atmospheric Sciences, Oregon State University, Corvallis, Oregon, USA

^{*}Correspondence: jiwoonp@uw.edu

conditions in which they are produced remain unclear (Tagliabue et al. 2017). Iron-binding ligands in seawater have been most commonly measured by competitive ligand exchange-adsorptive cathodic stripping voltammetry (CLE-ACSV; Gledhill and van den Berg 1994; Buck et al. 2012; Bundy et al. 2015). This electrochemical method groups ligands into classes operationally defined by their binding affinity for iron, with the L₁ class being the strongest iron-binding ligands and L₂ and below being progressively weaker ligands (Hunter and Boyd 2007; Gledhill and Buck 2012; Bundy et al. 2015). As the concentration of the L₁ ligand class is closely correlated to dissolved iron throughout the global ocean (Gledhill and Buck 2012; Buck et al. 2018), it is currently the main class of ligands represented in biogeochemical models of the iron cycle (Tagliabue et al. 2017). CLE-ACSV does not provide any information on the chemical structures of different ligands across classes, but combining these method with mass spectrometry allows direct characterization of individual ligand structures at the molecular level (Mawji et al. 2008; Boiteau et al. 2016; Bundy et al. 2018). The similarities between the iron binding strength of L₁ class ligands and that of siderophores suggest that a part of the L1 ligand pool may be made up of siderophores (Vraspir and Butler 2009).

Siderophores are low molecular weight, strong iron-binding molecules produced by microbes (Neilands 1981). More than 500 siderophores have been identified and isolated to date, mostly from bacteria and fungi cultures (Sandy and Butler 2009; Hider and Kong 2010). Siderophores are synthesized inside cells by either the nonribosomal peptide synthetase (NRPS) pathway or the NRPS-independent siderophore synthetase pathway and are secreted to the environment (Gulick 2017; Carroll and Moore 2018). Gram-negative bacteria use a combination of TonB-dependent outer membrane receptors and ATP-binding cassette transporters to transport iron-bound siderophores through the outer membrane into the periplasm and the cytoplasm (Krewulak and Vogel 2008). The ability to synthesize and transport siderophores varies widely between microbes: some microbes can produce one or more siderophores, some cannot produce siderophores themselves but possess the siderophore uptake machinery to use exogenous siderophore-bound iron, and some cannot produce or utilize siderophores (Sandy and Butler 2009; Gledhill and Buck 2012; Kramer et al. 2020). Siderophore production benefits its producers by decreasing the amount of available iron to other microbes that lack the ability to acquire siderophore-bound iron (Kramer et al. 2020). In addition, as siderophores can solubilize particulate iron to increase the amount of dissolved iron, they can alter the pool of bioavailable iron in the marine environment and shape the microbial community structure and composition (Kraemer et al. 2005; Kügler et al. 2020).

Multiple studies to date have measured picomolar concentrations of siderophores in surface and mesopelagic ocean waters (0–1500 m; Boiteau et al. 2016, 2019; Bundy et al. 2018). In these studies, characterized iron-siderophore complexes accounted for 0.2–10% of the total dissolved iron pool, which suggests that

siderophores can play a significant role in ocean iron cycling. Indeed, the prevalence of siderophore-based iron acquisition in the ocean has been demonstrated by genomic and transcriptomic surveys of marine communities. For instance, TonB-dependent outer membrane receptors involved in siderophore uptake were widespread among prokaryotes in the Global Ocean Survey (GOS) metagenomes (Hopkinson and Barbeau 2012; Tang et al. 2012; Toulza et al. 2012). In addition, siderophore uptake transcripts in the Southern Ocean were mostly derived from prokaryotes, particularly Gammaproteobacteria and Fibrobacteres-Chlorobi-Bacteroidetes groups, which suggest that prokaryotes may prefer the siderophore-mediated iron uptake pathway to ferrous and ferric iron transport pathways (Debeljak et al. 2019). Siderophore biosynthesis genes were detected less frequently and at a lower abundance from the GOS metagenomes than siderophore uptake genes, potentially because fewer siderophore synthesis genes were characterized and included in the search databases, or because most microbes cannot afford the expensive cost of siderophore production (Hopkinson and Barbeau 2012; Toulza et al. 2012). The combination of environmental genomic and transcriptomic surveys for siderophore biosynthesis and uptake genes can give important insights into siderophore biosynthesis or uptake potential, and further provide evidence for active production and cycling of siderophores in seawater. However, to our knowledge, no study to date has paired a genomics- and transcriptomics-based approach with chemical measurements of siderophore concentrations and distributions.

To examine possible chemical and biological controls of siderophore distributions, we measured dissolved siderophore concentrations across a basin-scale meridional transect at 158°W, from 23.5°N to 41.4°N in the North Pacific Ocean during two cruises in 2016 and 2017. In addition, to evaluate the impact of microbial activity on siderophore distribution, we first searched for a comprehensive set of siderophore synthesis and uptake genes and transcripts across both cruise transects, then further for a subset of three specific siderophore transporter genes.

Methods

Seawater collection

Samples were collected during the Gradients 1 cruise (KOK1606) on the R/V *Ka'imikai-O-Kanaloa* from 19 April 2016 to 03 May 2016 and the Gradients 2 cruise (MGL1704) on the R/V *Marcus G. Langseth* from 27 May 2017 to 13 June 2017. Samples were collected along 158°W, from 23.5°N to 37.5°N and 25.8°N to 41.4°N, respectively. Seawater samples for dissolved iron and siderophore analyses were collected using Niskin-X bottles with external Teflon-coated springs (General Oceanics) mounted on a trace metal-clean rosette and a nonmetallic line. Collection depths were preprogrammed to the autofire module (Seabird Scientific) and sample bottles were closed on the upcast while the rosette was moving through the water (\sim 20–30 m min⁻¹). Niskin-X

bottles were placed in a high efficiency particulate air (HEPA)-filtered clean space on board the ship prior to sub-sampling. Surface samples ($\sim 5~\text{m}$) were collected from a towed trace metal-clean "fish" (Vink et al. 2000) and sample bottles were filled inside a HEPA-filtered clean space.

Sea surface temperature and salinity were measured from thermosalinograph systems aboard each research vessel. Sample collection and analysis for nitrate plus nitrite (N + N), soluble reactive phosphorus (SRP), particulate organic carbon (POC) concentrations, and $\rm O_2/Ar$ -derived estimates of net community production (NCP) are described in Juranek et al. (2020).

Discrete samples for bacterial cell abundance measurements by flow cytometry were collected from surface water ($\sim 5\,\mathrm{m}$ depth), fixed with glutaraldehyde (0.25% final concentration) and analyzed with a BD Influx cell sorter equipped with a 488-nm laser. Data collection was triggered by forward light scatter (10% neutral density). Total bacteria counts were obtained by staining the sample with SYBR Green I (0.01% final concentration) for 20 min in the dark and detecting emission at 530 nm (40 nm bandpass). *Prochlorococcus* cell counts were determined on unstained samples based on forward scatter and chlorophyll fluorescence emission at 692 nm (40 nm bandpass). Heterotrophic bacteria abundance was calculated by subtracting *Prochlorococcus* counts from the total bacteria count (Marie et al. 1999).

Dissolved iron analyses

Surface seawater samples for dissolved trace metals were filtered through 0.2- μ m Supor membrane filters (Pall), and the filtrates were stored in 50-mL acid-cleaned polypropylene centrifuge tubes (VWR). Samples were analyzed after off-line preconcentration onto Nobias PA1 chelating resin at pH \sim 6.5 using the seaFAST-pico system (Lagerström et al. 2013). Samples were eluted in 10% nitric acid (Optima, Fisher Scientific) and analyzed on a Thermo Fisher Element 2 High-Resolution ICP-MS using the isotope dilution method (Pinedo-González et al. 2020). The accuracy of measured dissolved iron concentrations was evaluated by referencing to consensus values of a seawater reference standard (GEOTRACES GS) and are reported elsewhere (Gradoville et al. 2020; Pinedo-González et al. 2020).

Dissolved siderophore sample collection and analysis

Ten to 20 liters of $0.2~\mu m$ filtered (Acropak 200; Pall Corporation) seawater were collected from stations between $23.5^{\circ}N$ and $37.5^{\circ}N$ (Gradients 1) or between $29.5^{\circ}N$ and $41.4^{\circ}N$ (Gradients 2) from multiple depths between the surface and 400 m. The filtered seawater was pumped continuously at a flow rate of $18~mL~min^{-1}$ through a Bond Elut column (1 g ENV, 6 mL, Agilent Technologies) that had been previously cleaned with two column volumes of pH 2 Milli-Q water and two column volumes of Milli-Q water, and activated with two column volumes of trace metal clean methanol (Fisher

Scientific Optima or distilled methanol). After the sample solid phase extraction was completed, columns were washed with 12 mL of Milli-Q water and stored at -20°C for later analyses.

Prior to analysis in the laboratory, the Bond Elut columns were thawed, rinsed with two column volumes of Milli-Q water, and eluted using 13 mL of optima or distilled methanol. The eluents were dried down using a vacuum concentrator with a refrigerated vapor trap (Thermo Scientific) over 4-5 h, brought up to final volumes of 500 μL using Milli-Q water and stored in 2-mL low-density polyethylene vials. Multiple method blanks were prepared along with samples to ensure that the samples were not contaminated during extraction. All samples were analyzed using liquid chromatography coupled to inductively coupled plasma mass spectrometry (LC-ICP-MS) and to electrospray ionization mass spectrometry (LC-ESI-MS). For each analysis, 50 µL aliquots of each sample were spiked with $10 \,\mu\text{L}$ of $5 \,\mu\text{M}$ cyanocobalamin as an internal standard and were analyzed on a Dionex Ultimate 3000 liquid chromatography system with a polyetheretherketone ZORBAX-SB C18 column (0.5 \times 150 mm, 5 μ m, Agilent Technologies). Samples were separated using a flow rate of 50 µL min⁻¹ at 30°C and a 20 min gradient from 95% solvent A (Milli-Q water with 5 mM ammonium formate) and 5% solvent B (trace metal clean methanol with 5 mM ammonium formate) to 90% solvent B, followed by a 10 min isocratic step of 90% solvent B, then a 5 min gradient from 90% to 95% solvent B, an isocratic 5 min step at 95% solvent B, and a 15 min conditioning step at 5% solvent B prior to injecting the next sample. The same chromatography scheme was used both for the LC-ICP-MS and the LC-ESI-MS analyses (Boiteau et al. 2016; Bundy et al. 2018).

Samples were introduced from the LC to the ICP-MS (iCAP-RQ; Thermo Scientific) equipped with platinum sample and skimmer cones at a flow rate of $50 \,\mu\text{L}$ min⁻¹ via a PFA-ST nebulizer (Elemental Scientific) and a spray chamber at 2.7° C. A 10% oxygen flow was added to the sample gas to prevent deposition of organic materials on the sampler and skimmer cones. Measurements were made in kinetic energy discrimination mode with a helium collision gas at a flow rate of 3.8– $4.0 \,\text{mL} \,\text{min}^{-1}$. 56 Fe peaks were identified using in-house R scripts (Boiteau et al. 2016; Bundy et al. 2018), and siderophore concentrations were calculated from calibration curves of ferrioxamine E (Boiteau et al. 2016; Bundy et al. 2018).

To identify siderophores structurally, samples were further analyzed with an Orbitrap (Q-Exactive HF; Thermo Scientific) with the following instrument settings: 3.5 kV spray voltage, 320°C capillary temperature, 16 sheath gas, 3 auxiliary gas, and 1 sweep gas (arbitrary units), 90°C auxiliary gas heater temperature and S-lens RF level 65 MS^1 scans were collected in full positive mode with 120,000 mass resolution, 200-2000 m/z mass range, $1e^6 \text{ AGC}$ target, and 100 ms maximum injection time. $MS^2 \text{ scans}$ were collected in data-dependent $MS^2 \text{ (dd-MS}^2)$ mode with 30,000 mass resolution, 1.0 m/z isolation window, $2e^4 \text{ AGC}$ target, 100 ms maximum injection

time and 35% collision energy, and used an inclusion list containing known masses of ~ 300 siderophores (Supporting Information Table S1). Raw data files were converted to mzXML formats using MSConvert (Proteowizard) and processed via in-house R scripts using the XCMS package (Boiteau et al. 2016; Bundy et al. 2018). Cyanocobalamin peaks (m/z=678.291) in each extracted ion chromatogram were aligned to $^{59}\mathrm{Co}$ peaks in each ICP-MS chromatogram to account for differences in retention times. Siderophores were identified using exact masses of known siderophore compounds from MS 1 ($\pm~0.005~\mathrm{Da}$), then further identified by MS 2 fragmentation patterns when possible.

A confidence level was assigned to each mass feature based on the putative identification of each siderophore. The confidence levels were modeled after those used in metabolite identification (Sumner et al. 2007; Supporting Information Table S2). Level 1 is the highest level of confidence, for which MS² spectra of our samples were matched to spectra from other publications (10 compounds). As MS² spectra were not obtained on all samples, we matched exact masses (\pm 0.005 Da) and retention time (\pm 0.5 min for Gradients 1 samples and \pm 1 min for Gradients 2 samples) from samples with MS² data to identify compounds in samples with no MS² data and annotated those compounds as level 2 (13 compounds). We used a larger retention time tolerance window for samples from Gradients 2 cruises to account for instrument variability, as these samples were analyzed at two different institutions over the course of a year. Compounds that had MS² spectra matching in silico MS² spectra (CFM-ID and MetFrag) were annotated as level 3 (3 compounds; Ruttkies et al. 2016; Djoumbou-Feunang et al. 2019). Finally, compounds were annotated as level 4 if they were identified as a putative siderophore based on MS¹ but there was no MS² spectra available for comparison, or if the obtained MS² spectra did not agree with the in silico predicted MS² spectra (53 compounds).

Metagenomic and metatranscriptomic sampling and processing

During both cruises, seawater samples for metagenomes and metatranscriptomes were collected either from the flow-through system or from a CTD rosette at 15 m depth. In each instance, 6–10 liters of seawater were passed through a nitex prefilter (200- μ m mesh for Gradients 1 and 100- μ m mesh for Gradients 2) followed by sequential filtration through a 3- and 0.2- μ m polycarbonate filters using a peristaltic pump. This collection scheme yielded two size classes (0.2–3 μ m and 3–100 or 200 μ m). In this study, we focused on the 0.2–3 μ m size fraction that includes "free-living" bacterial communities. Filters were frozen in liquid nitrogen and stored at -80° C until further processing.

Samples from the $0.2–3~\mu m$ size fraction were used to construct sequencing libraries. To generate quantitative read inventories, internal standards of *Thermus thermophilus* genomic DNA for metagenomes and a set of 14 synthetic internal mRNA standards for metatranscriptomes (Satinsky et al. 2013;

Durham et al. 2019) that included eight standards synthesized with polyA tails to mimic eukaryotic mRNA and six without polyA tails to mimic prokaryotic mRNAs were added in known concentrations prior to nucleic acid extraction. Specifically, 5.2×10^6 copies of T. thermophilus genomic DNA and 1.358×10^{10} copies of each prokaryotic mRNA standard were added. The number of sequenced reads recovered from the internal standards was used to calculate a normalization factor for each sample as previously described, and we used only the prokaryotic mRNA standards in our analysis (Satinsky et al. 2013). DNA was extracted using phenol: chloroform following enzymatic cell lysis (Boström et al. 2004), fragmented to \sim 600 bp and used to construct Nextera DNA Flex libraries. Total RNA was extracted using the ToTALLY RNA kit (Invitrogen) for Gradients 1 samples and the Direct-zol RNA MiniPrep kit (Zymo Research) for Gradients 2 samples, and processed as described previously (Durham et al. 2019). Briefly, RNA extracts were treated with DNase, and rRNAs were removed using Illumina's Bacteria and Yeast Ribo-Zero rRNA Removal Kits. The rRNA-depleted RNA was cleaned using the Zymo RNA Clean and Concentrator Kit. Purified, depleted RNA was then sheared to \sim 225 bp fragments and used to construct TruSeq cDNA libraries according to the Illumina TruSeq® RNA Sample Preparation v2 Guide. Metagenomic and metatranscriptomic libraries were sequenced with the Illumina NovaSeq 6000 sequencing platform using the S4 flow cell with paired-end (2 \times 150) chemistry.

Metagenome and metatranscriptome analysis

Sequence reads from metagenomes were quality controlled using BBDuk v38.22 with the settings ktrim = r, k = 23, mink = 8, hdist = 1, qtrim = rl, trimq = 20, minlen = 50, tpe, mag = 10. Reads were then assembled into contigs de novo using SPAdes v3.13.1 using the --meta flag with kmer lengths of 33, 55, and 77. Proteins translated from metagenomic contigs were searched against a comprehensive library of profile hidden Markov models (HMMs) for siderophore biosynthesis and uptake genes (Garber et al. 2020) using hmmsearch (parameters: -T 50) with the HMMER package v2.1 (Eddy 2011). Gene abundances in copies per liter of seawater were obtained by normalizing the sequence reads to that of the internal standard. Kaiju v1.7.0 was used to taxonomically classify the retrieved protein sequences related to siderophore biosynthesis and transport genes using the MARMICRODB database using the default settings (Menzel et al. 2016; Hogle 2019). Raw Illumina metatranscriptome data were quality controlled with trimmomatic v0.36 (Bolger et al. 2014) using the parameters MAXINFO:135:0.5, LEADING:3, TRAILING:3, MINLEN:60, and AVGQUAL:20, and matching read pairs were merged using flash v1.2.11 (Magoc and Salzberg 2011) with parameters -r 150 -f 250 -s 25. Sequences were pooled for each sampling station in the two cruises, and the pooled samples were assembled using Trinity v2.3.2 (Grabherr et al. 2011) with the following parameters: -normalize_reads min_kmer_cov 2 -min_contig_length 300. The resulting contigs

were translated in six frames with segret and transeq vEMBOSS:6.6.0.0 (Rice et al. 2000) using standard genetic code. The longest reading frame for each contig was retained for further analysis, and potential best frame contigs with > 100 uninterrupted amino acids were retained for analysis. The translated assemblies were merged and clustered for each cruise separately at the 99% identity level using linclust within the MMseqs2 package version 31e25cb081a874f225d443eec307a6 254f06a291 (Steinegger and Söding 2018) with parameters -min_seq_id 0.99. The contigs for each individual sample in the two cruises were counted by alignment of contig nucleotide sequences to the paired-end reads using kallisto v0.43.1 (Bray et al. 2016), with parameters quant -b 100. Transcriptomic raw read counts were normalized by recovery of internal mRNA standards to estimate transcript abundance in total transcripts per liter. Kaiju v1.7.0 was used to taxonomically annotate the counted contigs using the MARMICRODB database (Menzel et al. 2016; Hogle 2019). Translated protein sequences were searched against the same library of profile HMMs used for metagenome analysis using hmmsearch with the HMMER package v2.1 (Eddy 2011) with identical parameters.

We further searched for translated reads corresponding to outer membrane transporters of three siderophores ferrioxamine (FoxA and DesA), amphibactin (FhuA), and salmochelin (FepA and IroN). Full-length, experimentally verified protein sequences from reference genomes (Supporting Information Table S3) were used as queries to identify putative orthologs in translated protein sequences from marine microbial genomes and transcriptome assemblies compiled in a custom marine reference database (Coesel et al. 2021) using BLASTp v2.2.31. Genomes and transcriptomes used in this database were derived from Joint Genome Institute, National Center for Biotechnology Information (NCBI), and the Marine Microbial Eukaryote Transcriptome Sequence Project (Keeling et al. 2014), and a complete list is available in Coesel et al. (2021). Marine sequences retrieved from the BLASTp search were clustered using usearch (Edgar 2010) and aligned using MAFFT v7 with the E-ISN-I algorithm (Katoh and Standley, 2013). The alignment was trimmed using trimAl v1.2 using – gt 0.05 –resoverlap 0.5 –seqoverlap 50 options (Capella-Gutierrez et al. 2009). The trimmed alignment file was converted to PHYLIP format, and the best-fit amino acid substitution matrix, among-site rate heterogeneity model, and observed amino acid frequency were determined using ProtTest 3 software (Darriba et al. 2011). A maximum-likelihood phylogenetic reference tree was built using RAxML v8 (Stamatakis 2014), and only those sequences that clustered with experimentally verified enzymes were considered putative homologs. These phylogenetic reference trees served as scaffolds to recruit translated environmental metatranscriptomic reads. An HMM profile was constructed from each reference alignment using hmmbuild, followed by transcript identification and alignment to the reference using hmmsearch (parameters: -T 40 -incT 40) and hmmalign, respectively, with the HMMER package v2.1

(Eddy 2011). NCBI taxonomy was assigned to each environmental sequence using pplacer v1.1.alpha19-0-g807f6f3 (Matsen et al. 2010) based on the read placement with the best maximum likelihood score to the reference tree (parameters: --keep-at-most 1 -max-pend 0.7). Due to the high similarity among ferrioxamine, amphibactin, and ferrichrome transporter sequences (28-55%) and between salmochelin and enterobactin transporter sequences (40-92%), each group of transporter homologs was combined to construct a single reference tree (Supporting Information Fig. S1; Table S3). For the combined ferrioxamine-amphibactin-ferrichrome transporters, we report sequences most closely related to the experimentally verified sequences separately from those more distantly related (Supporting Information Fig. S1; Table S3). Read counts from triplicate samples were averaged at each latitude. To determine if the mean read counts for each taxonomic group were significantly different between latitudes, a one-way ANOVA and a post hoc Tukey multiple comparison test was applied.

Results

Water properties along the study transects

The two cruises crossed three distinct regions of the North Pacific Ocean: the North Pacific Subtropical Gyre (NPSG), the North Pacific Transition Zone (NPTZ), and the North Pacific Subarctic Frontal Zone (SAFZ; Fig. 1a). The NPTZ has previously been defined based on latitudinal gradients of physical and biological features (Roden 1991; Polovina et al. 2001). The southern boundary of the NPTZ, or the North Pacific subtropical front, generally corresponds to the 34.8 isohaline and the 18°C isotherm (Roden 1991). The transition zone chlorophyll front (TZCF) is a dynamic feature between the NPSG and the subarctic gyre, and is operationally defined by surface chlorophyll a concentrations of 0.2 mg m^{-3} (Polovina et al. 2001). The TZCF does not always coincide with the physical definition of the NPTZ, as it migrates seasonally by $\sim 10^\circ$ in latitude, due to strong seasonal gradients in nutrients, light, and shifts in phytoplankton composition (Follett et al. 2021).

In both cruise transects, we observed decreases in sea surface temperature and salinity as we transited northward (Fig. 1b,c). The second derivative of surface salinity was used to determine the position of the North Pacific subtropical front, which was 30.7°N in April 2016 and 32.8°N in June 2017 (Gradoville et al. 2020; Follett et al. 2021). In addition, the subarctic salinity front was only crossed in June 2017, and this front was located at 38.0°N based on the 33.8 isohaline (Roden 1991; Gradoville et al. 2020). These frontal locations will be used in the remainder of this work when discussing the NPSG, the NPTZ, and the SAFZ (Fig. 1).

Strong latitudinal trends in surface nutrient inventories were observed in both cruises, with N+N and SRP concentrations both increasing across the NPSG to NPTZ or SAFZ by up to tenfold (Juranek et al. 2020; Fig. 1d,e). Along with changes in nutrients, latitudinal changes in productivity and biomass

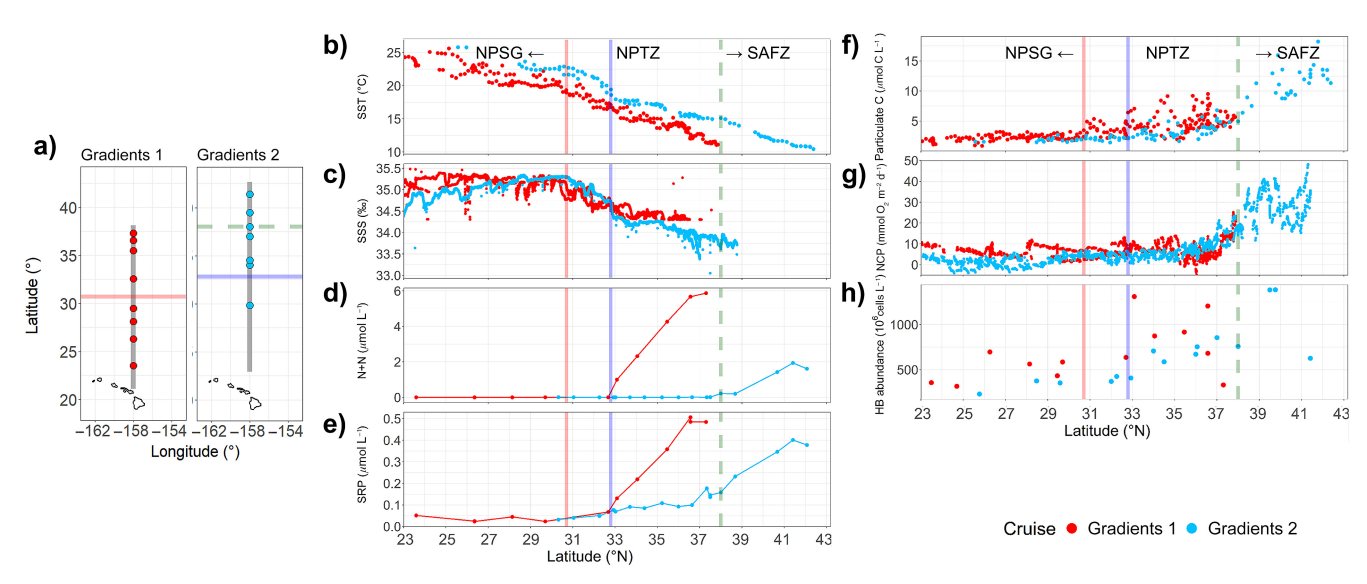


Fig. 1. Physical, chemical, and biological properties measured along the two cruise transects. (a) Transects of Gradients 1 (red) and 2 (blue) cruises, (b) sea surface temperature (SST), (c) sea surface salinity (SSS), (d) nitrate and nitrite (N + N) concentrations, (e) soluble reactive phosphorus (SRP) concentrations, (f) particulate organic carbon (POC) concentrations, (g) O_2 /Ar-derived estimates of net community production (NCP), and (h) heterotrophic bacterial abundances from Gradients 1 (red) and 2 (blue) cruises. Vertical red and blue solid lines indicate location of subtropical fronts from Gradients 1 and 2 cruises, respectively; green dashed line indicates location of the subarctic front from Gradients 2.

were also observed. Both particulate organic carbon (POC) and O_2/Ar -derived NCP sharply increased across the TZCF, which was located at 33.0°N in April 2016 and 36.2°N in June 2017, and reached a maximum at the northern-most stations (Juranek et al. 2020; Fig. 1f,g). Heterotrophic bacterial cell abundances at the surface also increased with latitude by tenfold across both transects (Fig. 1h).

Surface dissolved iron concentrations showed different latitudinal trends between the two years (Fig. 2a). In April 2016, surface dissolved iron concentrations were highest in the NPSG (0.13-0.31 nM) and generally decreased with increasing latitude, whereas in June 2017, surface dissolved iron concentrations were highest in the NPTZ (0.20-0.51 nM; Pinedo-González et al. 2020). The peak in dissolved iron concentrations at 35°N in June 2017 was interpreted to be due to atmospheric deposition of anthropogenic aerosols from Asia, based on the isotopic composition of dissolved iron and lead (Pinedo-González et al. 2020). The difference in iron distributions between the two cruises was likely caused by the seasonal supply of aerosol-derived iron to the North Pacific Ocean, as depth-averaged satellite observations of aerosol optical depth show higher aerosol concentrations over the region of our cruise transect in spring to early summer (March-July; Supporting Information Fig. S2).

Siderophore distributions in the North Pacific

Dissolved siderophore concentrations in surface waters (0–25 m) differed between the April 2016 and June 2017 transects (Fig. 2b). In April 2016, surface siderophore concentrations (1.4 \pm 1.3 pM) were relatively uniform across the transect,

with no statistically significant difference between the NPSG (1.4 \pm 1.0 pM) and the NPTZ (1.4 \pm 1.7 pM; Mann–Whitney *U*-test, p=1). In contrast, surface siderophore concentrations in June 2017 were higher and more variable than in 2016, with average concentrations of 14.3 \pm 25.9 pM. In addition, siderophore concentrations in the NPTZ (9.3 \pm 4.1 pM) were higher than concentrations in the SAFZ (3.0 \pm 1.7 pM; Mann–Whitney *U*-test, p=0.06).

Siderophore concentrations below the surface (25–400 m) were not significantly different from surface concentrations in either 2016 or 2017 (Mann–Whitney *U*-test, p=0.46 and 0.11, respectively), nor significantly different between the NPSG (1.4 \pm 1.6 pM) than in the NPTZ (0.7 \pm 0.7 pM) in April 2016 or between the NPTZ (12.8 \pm 23.5 pM) and SAFZ (3.3 \pm 3.1 pM) in June 2017 (Mann–Whitney *U*-test, p=0.35 and 0.13; Fig. 3b).

Siderophore identities in the North Pacific

Among the siderophores we identified with high confidence (levels 1–3) in April 2016 (8 siderophores) and June 2017 (10 siderophores), ferrioxamines were the most common type of siderophore detected and were found in samples from Gradients 1 (Fig. 4) and Gradients 2 (Fig. 5). Ferrioxamine E and G1 were detected in both years (Figs. 4a,b, 5a,b), whereas ferrioxamine B was only detected in April 2016 (Fig. 4c). Most ferrioxamines were complexed to iron, however, in 2 out of 28 ferrioxamine identifications, both iron-bound and apo-(iron-free) ferrioxamine E were detected, with concentrations of apo-ferrioxamine E approximately a tenth of iron-bound ferrioxamine E. Different types of ferrioxamines were found

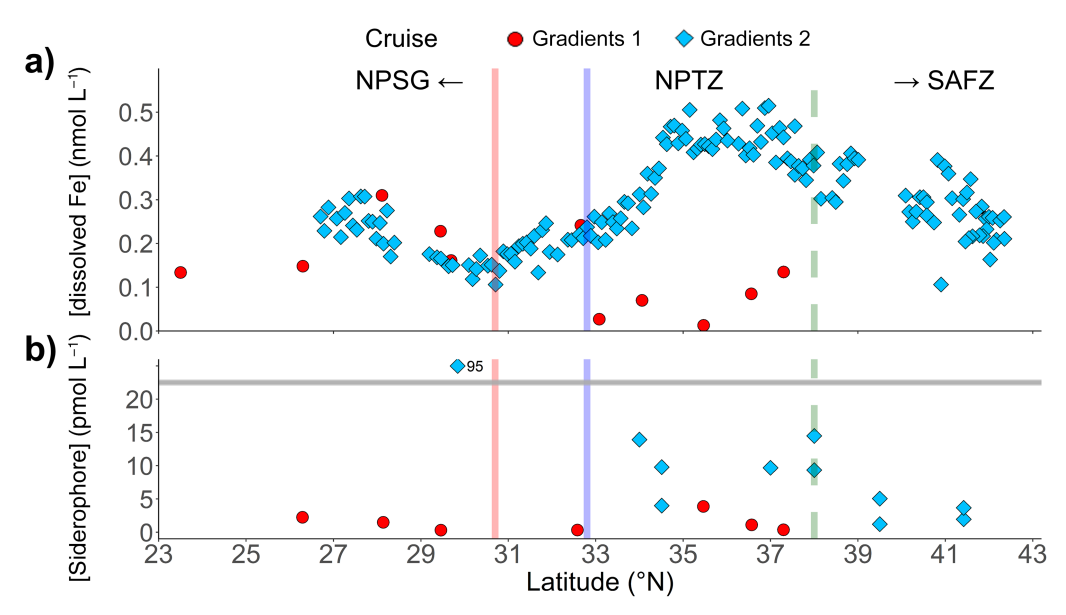


Fig. 2. Dissolved iron and siderophore concentrations in surface waters along the two cruise transects. (a) Dissolved iron concentrations in surface waters collected with a trace metal clean towfish from Gradients 1 (red) and 2 (blue). (b) Siderophore concentrations in surface waters (0–25 m) from Gradients 1 (red) and 2 (blue). One data point from Gradients 2 had siderophore concentrations outside the *y*-axis range of the plot (above the horizontal gray *y*-axis break line), and its concentrations is noted at the right of the data point. Vertical red and blue solid lines indicate location of subtropical fronts from Gradients 1 and 2 cruises, respectively; green dashed line indicates location of the subarctic front from Gradients 2.

across all depths in both the NPSG and the NPTZ, but not in the SAFZ. In addition, multiple types of ferrioxamines were often detected concurrently in a single location. We also detected a suite of amphibactins (D, E, H, T) complexed to iron in June 2017, and these were mostly found in the NPSG and the southern part of the NPTZ ($\sim 35^{\circ}$ N), except amphibactin E, which was found across the full range of NPTZ (Fig. 5c–f).

In addition to ferrioxamines and amphibactins, we also detected several photoreactive siderophores in their iron-free forms, based on their MS¹ and MS² fragmentation data with confidence levels 1–3. Apo forms of synechobactin c12 and c13 were detected consistently across the cruise transects in April 2016 and June 2017, respectively (Figs. 4e, 5h), and were mostly confined to surface waters (0–150 m). Iron-free petrobactin, another photolabile siderophore, was detected in

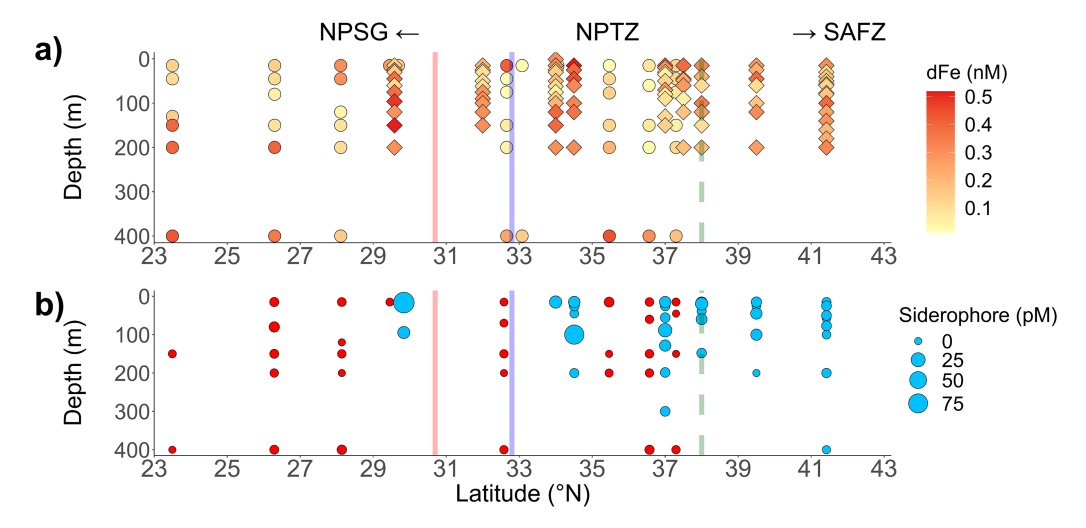


Fig. 3. Depth profiles of dissolved iron and siderophore concentrations along the two cruise transects. (a) Depth profiles of dissolved iron concentrations from Gradients 1 (circles) and 2 (diamonds) across 0–400 m from CTD casts. (b) Depth profiles of dissolved siderophore concentrations from Gradients 1 (red) and 2 (blue) across 0–400 m. Point sizes are proportional to siderophore concentrations. Vertical red and blue solid lines indicate location of subtropical fronts from Gradients 1 and 2 cruises, respectively; green dashed line indicates the location of the subarctic front from Gradients 2.

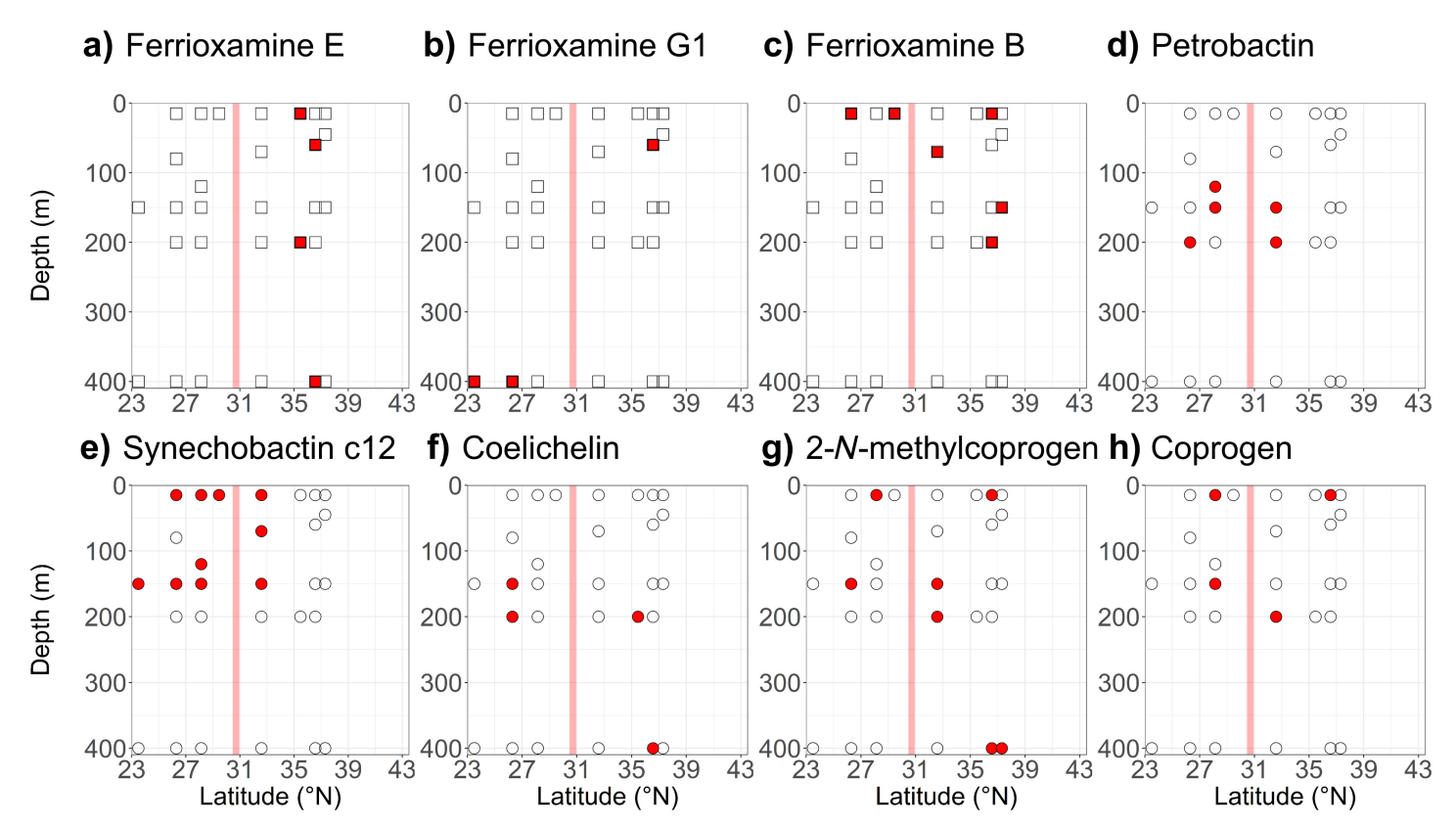


Fig. 4. Distributions of siderophores identified with confidence levels 1–3 from the Gradients 1 cruise. Red-filled squares (Fe-bound form) and circles (Fe-free form) indicate sampling locations where each siderophore was detected; blank squares and circles show sampling locations where siderophores were not detected. Vertical red solid line indicates the location of the subtropical front from Gradients 1.

April 2016, at depths between 100 and 400 m (Fig. 4d). North of the subarctic salinity front in June 2017, we also found apo forms of schizokinen (Fig. 5g), another siderophore that may be photoreactive given the α -hydroxy-carboxylic acid group in its structure, although its photoreactivity has not yet been confirmed (Årstøl and Hohmann-Marriott 2019).

In addition, we detected multiple siderophores not previously detected in the marine environment. Apo forms of heterobactin B were found in north of the subarctic salinity front in 2017 (Fig. 5i). We also found siderophores known to be produced by marine or terrestrial fungi (coprogen and 2-*N*-methylcoprogen) sporadically distributed across the transect.

Siderophore-related genes and transcripts

We searched for siderophore synthesis and transport genes and transcripts in the metagenomic and metatranscriptomic datasets collected from surface waters during both cruises. Siderophore synthesis genes were detected at abundances of 2.63 ± 0.93 and 5.98 ± 3.15 million copies L^{-1} from the 2016 and 2017 cruises, respectively, while siderophore transport genes were detected at abundances of 1.98 ± 0.71 and 4.22 ± 2.25 million copies L^{-1} from the 2016 and 2017 cruises, respectively (Fig. 6a). Both siderophore synthesis and transport gene abundances from each cruise increased significantly with

latitude (simple linear regression analysis, p < 0.05, R^2 ranging from 0.17 to 0.25). Among 82 and 95 siderophore transport and synthesis gene families we searched for, PirA and VabA gene families were most frequently detected across both cruises (Supporting Information Fig. S3). Siderophore synthesis genes were derived primarily from Gammaproteobacteria (20–42%) and Alphaproteobacteria (30–50%), while siderophore transport genes were derived primarily from Gammaproteobacteria (20–57%), Alphaproteobacteria (13–35%), and Bacteroidetes/Chlorobi group (3–29%; Supporting Information Fig. S4).

A total of 23.6–277 and 65.0–3547 million reads L^{-1} of siderophore synthesis transcripts were detected from the 2016 and 2017 cruises, respectively, while 155–785 and 160–3866 million reads L^{-1} of siderophore uptake transcripts were detected from the 2016 and 2017 cruises, respectively (Fig. 6b). Both siderophore synthesis and transport transcript abundances from the 2016 cruise were positively correlated with latitude (simple linear regression analysis, p < 0.05, R^2 ranging from 0.75 to 0.83), while those from the 2017 cruise were not significantly positively correlated with latitude (simple linear regression analysis, p = 0.13–0.19, R^2 ranging from 0.20 to 0.26). Similar to the search results from metagenomes, PirA and VabA were also the dominant siderophore uptake and synthesis gene families detected from the metatranscriptome

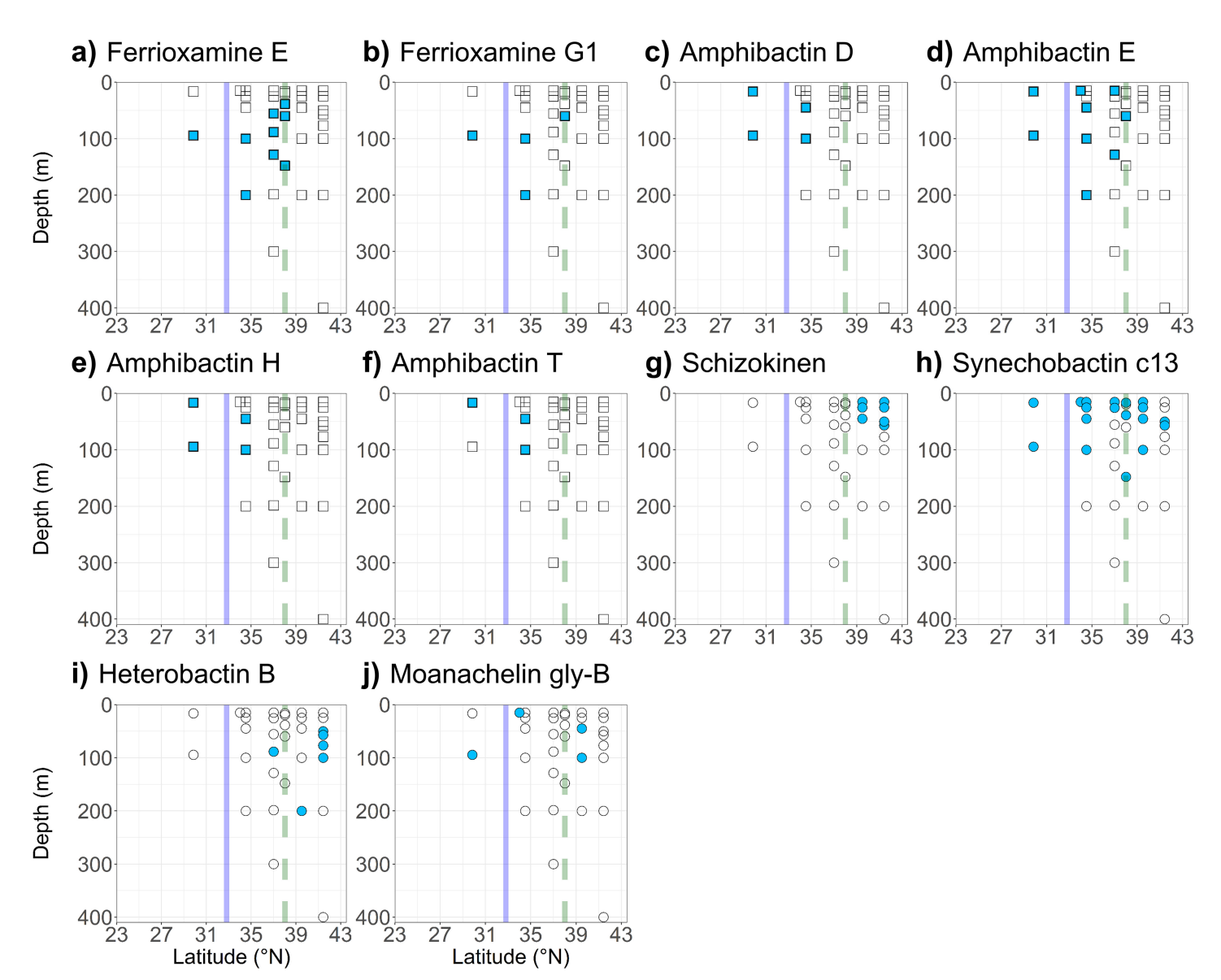
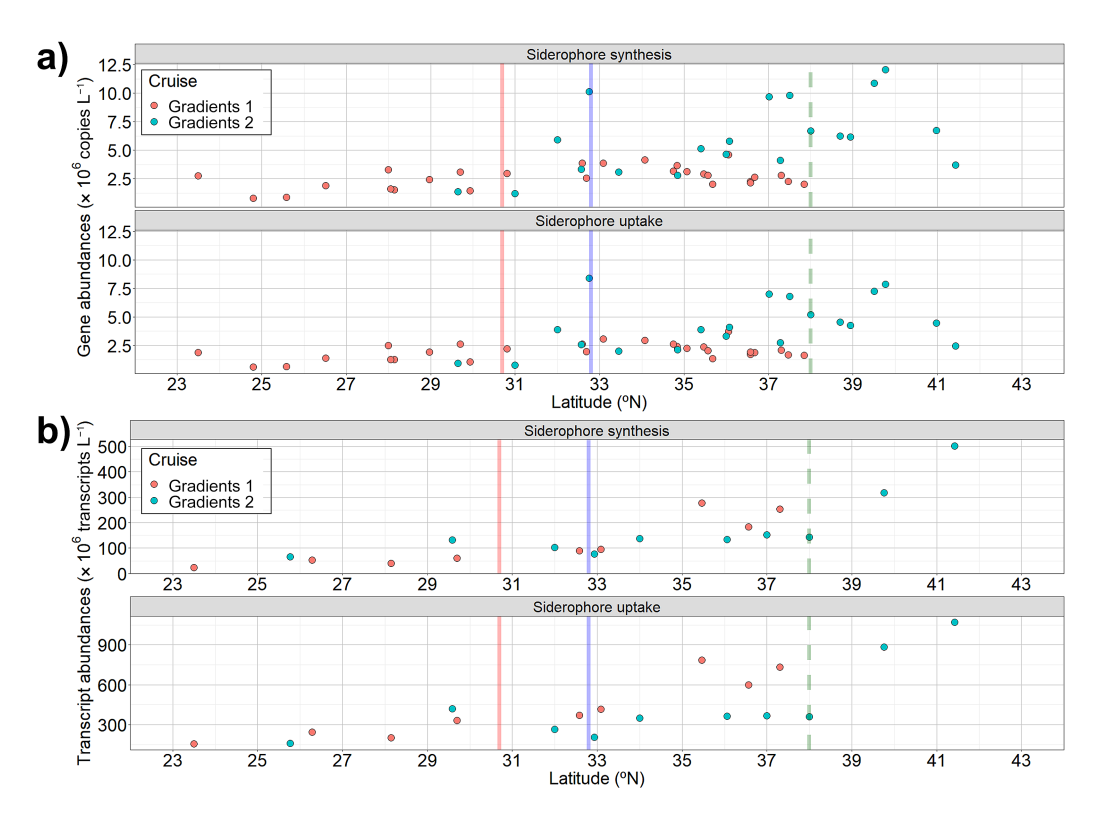


Fig. 5. Distributions of siderophores identified with confidence levels 1–3 from the Gradients 2 cruise. Blue-filled squares (Fe-bound form) and circles (Fe-free form) indicate sampling locations where each siderophore was detected; blank squares and circles show sampling locations where siderophores were not detected. Vertical blue solid line and the green dashed line indicate location of the subtropical front and the subarctic front from Gradients 2.

(Supporting Information Fig. S5). No individual siderophore transport or synthesis gene families were found to be clustered at specific latitudes (Supporting Information Figs. S3, S5). Siderophore synthesis and transport transcripts were also derived from the same microbial groups that possessed siderophore synthesis and transport genes. Gammaproteobacteria (15–59%) and Alphaproteobacteria (4–35%) produced most of siderophore synthesis transcripts, while Gammaproteobacteria (26–75%), Alphaproteobacteria (3–15%) and Bacteroidetes/Chlorobi group (7–63%) contributed most to siderophore uptake transcripts (Supporting Information Fig. S6).

To further examine which taxa may be actively cycling individual siderophore compounds along the cruise transects,

we analyzed transcript abundances for homologs of three outer membrane siderophore transporters—ferrioxamine and amphibactin (foxA, desA, fhuA) and salmochelin (fepA, iroN). These outer membrane transporters were chosen as these compounds were detected during both cruises, and outer membrane transporters for these siderophores have been characterized in multiple gammaproteobacterial species. We note that transporter homologs identified in marine microbial reference organisms for ferrioxamine, amphibactin, and ferrichrome, or for salmochelin and enterobactin, could not be distinguished from one another due to their high sequence similarity (Supporting Information Fig. S1; Table S3). Therefore, here we report a combined transcript abundance for the



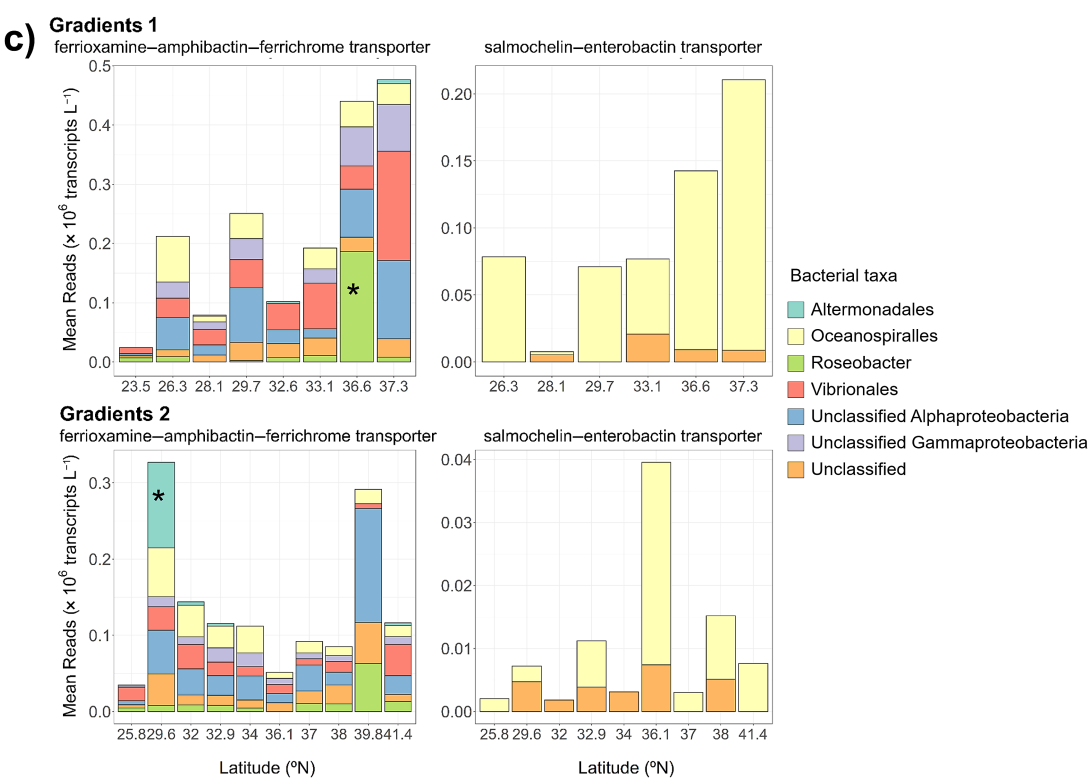


Fig. 6. Siderophore synthesis and uptake genes and transcripts abundances across the two cruise transects. (a) Mean abundances (10⁶ copies per liter of seawater) of siderophore synthesis and uptake genes in surface waters across latitude for Gradients 1 (red) and 2 (blue) cruises. Vertical red and blue solid lines indicate location of subtropical fronts from Gradients 1 and 2 cruises, respectively; green dashed line indicates the location of the subarctic front from Gradients 2. (b) Mean abundances (10⁶ copies per liter of seawater) of siderophore synthesis and uptake transcripts in surface waters across (Figure legend continues on next page.)

transporter homologs, though we also separated transcript inventories for the ferrioxamine–amphibactin–ferrichrome transporter signal based on phylogeny with experimentally verified sequences (Supporting Information Fig. S7).

The siderophore transporter homologs were transcribed by taxa belonging predominantly to Alphaproteobacteria and Gammaproteobacteria (Fig. 6c), groups that also encoded most of siderophore transport genes. From both cruises, the alphaproteobacterial Roseobacter group (10–13%) and gammaproteobacterial order Vibrionales (20–30%) contributed most to the total inventory of ferrioxamine–amphibactin–ferrichrome transporter transcripts. Mean transcript abundances of ferrioxamine–amphibactin–ferrichrome homologs differed significantly (one-way ANOVA and post hoc Tukey test) between Roseobacter at 36.6°N in 2016 and Altermonadales at 29.6°N in 2017 and other latitudes (Fig. 6c; p < 0.01). The gammaproteobacterial order Oceanospiralles (29–100%) was the major contributor to total salmochelin–enterobactin transporter transcript abundances (Fig. 6c).

Discussion

Siderophore distributions in the North Pacific

Our dataset greatly expands currently available measurements of dissolved siderophores in the ocean, as previous work has been confined to few depth profiles or has focused on surface waters. We found that dissolved siderophores were widely distributed throughout the North Pacific, both in surface waters and throughout the upper mesopelagic (down to 400 m), with concentrations comparable to those from earlier studies (0.3-20 pM; Boiteau et al. 2016; Boiteau et al. 2019; Bundy et al. 2018). Two data points at 29.8°N, 16.5 m depth and 37°N, 100 m depth had unusually high concentrations (95.2 and 77.7 pM, respectively). As all of our dissolved siderophore concentrations are likely representative of a snapshot in time and space, we may have sampled a water mass with a cluster of siderophore-producing microbes or with recently accumulated siderophores from cell death. Excluding these two points, dissolved siderophores accounted for $2.4\% \pm 5.4\%$ (or 0-30%) of the total dissolved iron pool across the North Pacific, suggesting that siderophores are an important component of the iron-binding ligand pool.

Elevated surface siderophore concentrations in the NPTZ in June 2017 may have been caused by higher siderophore production in this area. Although a direct correlation between surface siderophore concentrations and heterotrophic bacteria abundance has been observed previously (Mawji et al. 2008),

we did not find a strong correlation between surface siderophore concentrations and phytoplankton or bacterial biomass (including POC and heterotrophic bacteria cell abundances) or NCP (Figs. 1f-h, 2b). However, high siderophore concentrations in the NPTZ in June 2017 coincided with a large input of anthropogenic dust to this region (Pinedo-González et al. 2020), and it may be that this external dust input triggered the observed siderophore production. Only a small fraction of dust deposited in the ocean dissolves (approximately 2% but highly variable; Baker and Croot 2010), but siderophores can significantly increase the solubility of iron-bearing minerals in dust, such as iron oxides and clay minerals, so that Fe(III) from minerals are released and become available for microbial uptake (Kraemer et al. 2005; Parrello et al. 2016). A previous study in the Mediterranean Sea found a positive relationship between the fraction of iron released from dust particles and iron-binding ligand concentrations, with highest dust-derived iron and ligand concentrations in May and June and relative to other months (Wagener et al. 2008). Transient supply of excess iron can result in rapid production and release of siderophores over timescales of days, in order to relieve bacteria from the metabolically costly process of producing siderophores under iron stress (Adly et al. 2015). Therefore, high eolian dust supply to the North Pacific may have stimulated the microbial communities to increase siderophore production to mobilize and opportunistically take up iron. However, since the dissolved siderophore pool size depends both on siderophore production and release and on siderophore losses through uptake and degradation, different siderophore loss terms across our study sites are likely also contributing to the observed siderophore concentrations. Estimates of the total siderophore pool size (including the particulate intracellular siderophore pool) or metabolic fluxes of siderophore secretion and uptake are necessary to fully understand how the observed siderophore distribution patterns are being shaped by microbes.

To explore possible environmental drivers of siderophore distributions, including dissolved iron distributions, we also performed a logistic regression analysis using multiple environmental variables to see if any of the variables could successfully predict siderophore distribution. The regression results suggested that latitude was the most effective predictor of siderophore presence, which suggests that siderophore distributions are likely controlled by a combination of physical, chemical and biological factors (see Supporting Information).

Siderophores were also detected below the surface ocean from both years, despite decreased heterotrophic bacterial

(Figure legend continued from previous page.)

latitude for Gradients 1 (red) and 2 (blue) cruises in units of 10^6 copies per liter of seawater. Vertical red and blue solid lines indicate location of subtropical fronts from Gradients 1 and 2 cruises, respectively; green dashed line indicates the location of the subarctic front from Gradients 2. (**c**) Mean abundances (10^6 transcripts per liter of seawater) of ferrioxamine-amphibactin-ferrichrome and salmochelin-enterobactin uptake transcript homologs in surface waters from Gradients 1 and 2 cruises. Stars indicate taxonomic groups that significantly changed transporter transcript abundances at specific latitudes as determined by the multiple comparison test (p < 0.05).

abundances and increased dissolved iron concentrations with depth (Supporting Information Fig. S8; Fig. 3a). In the upper mesopelagic waters (150–400 m), siderophores make up $0.7\% \pm 0.8\%$ (or 0–3%) of the total dissolved iron pool. However, previous work found that heterotrophic bacteria from 150 m depth produced siderophores upon addition of in situ sinking particles, suggesting that bacteria are using iron in the sinking particles during regeneration by actively producing and cycling siderophores below the euphotic zone (Bundy et al. 2018). Therefore, while the dissolved siderophore pool size is smaller in the upper mesopelagic relative to the surface waters by up to an order of magnitude, heterotrophic bacteria at depth may be more actively cycling siderophores.

Siderophore identities in the North Pacific

Overall, we observed a wide variety of siderophores with litcompositional overlap between the tle cruises. Ferrioxamines—one of the most commonly detected siderophores in seawater to date—were the only siderophores that were detected on both cruises and in both the NPSG and NPTZ, regions with relatively high iron compared to the SAFZ (Figs. 4a-c, 5a,b). These observations generally agree with previously known distributions of ferrioxamines in iron-replete waters, such as coastal upwelling systems in Southern California and Peru, subtropical North Pacific, and the mid-latitude North Atlantic (Mawji et al. 2008; Boiteau et al. 2016, 2019). The abundances of ferrioxamines in iron-rich waters have been attributed to their extremely strong affinities to iron, which allows bacteria that can utilize ferrioxamines to efficiently compete for iron from dust or sedimentary sources (Mawji et al. 2008; Bundy et al. 2018; Boiteau et al. 2019).

Amphibactins are hydroxamate siderophores with amphiphilic tails that are also frequently detected in seawater. They were found in the NPSG and the southern part of the NPTZ (~ 35° N) in June 2017 (Fig. 5c-f). Earlier studies detected amphibactins mostly in iron-limited waters such as the eastern tropical Pacific and offshore of the California Current System (Boiteau et al. 2016, 2019). In particular, Boiteau et al. (2016) observed a marked shift from ferrioxamines in the high iron coastal region to amphibactins in the equatorial Pacific HNLC and hypothesized that amphiphilic siderophores, which can partition into the cell membrane, were favored in the HNLC to minimize diffusive losses of the siderophore in this iron-limited region. However, as amphibactins have also been observed in the NPSG (Bundy et al. 2018), their distributions may be driven not only by dissolved iron concentrations, but also by the distribution of various amphibactin-producing and consuming bacterial taxa, including many strains of Vibrio, the hydrocarbon-degrading Alcanivorax and nitrogen-fixing Azotobacter (Martinez et al. 2003; Kem et al. 2014; Zhang et al. 2019).

In addition to iron-bound ferrioxamines and amphibactins, we detected and identified several photoreactive siderophores in the iron-free form. These siderophores may not have been

routinely detected due to a previous focus on iron-bound compounds. Iron-free forms of synechobactin and schizokinen were found primarily in surface waters (0-200 m; Figs. 4e, 5g,h). As known producers of synechobactin and schizokinen include Synechococcus and Anabaena species, and as ironsynechobactin complexes can break down within a few hours when exposed to natural sunlight (Årstøl and Hohmann-Marriott 2019), the presence of synechobactins schizokinen in surface waters implies active production of photoreactive siderophores in the surface ocean. In contrast, the iron-free form of petrobactin was only detected below the surface ocean (100-400 m). The absence of iron-free petrobactin in surface waters may be due to photooxidation of the catecholate moieties on petrobactin (opposed to lightresistant hydroxamate moieties on synechobactin and schizokinen; Barbeau et al. 2003). Photoreactive siderophores have important implications for iron bioavailability, as photolysis of iron-siderophore complexes results in the reduction of Fe(III) to Fe(II), which in turn may become available for marine organisms that cannot take up iron bound to siderophores (Barbeau et al. 2003). Thus, further exploration of photoactive siderophores, especially in the surface ocean, may reveal their importance to marine carbon and iron cycling.

We also putatively identified heterobactin B and some fungi-derived siderophores, but much less is known about the production of these compounds. To date, heterobactins have been shown to be produced by several strains of *Rhodococcus* (Carrano et al. 2001), a genus of gram-positive bacteria related to *Mycobacterium*, although little is known about the genetically diverse *Rhodococcus* in the marine environment. Siderophore production by marine fungi has also not been well documented. Siderophores produced by fungi characterized to date are mostly hydroxamate siderophores (Holinsworth and Martin 2009). Marine fungi appear to produce higher concentrations of siderophores than their terrestrial counterparts (Baakza et al. 2004); however, the importance of these siderophores in oceanic iron cycling remains unclear.

Overall, we observed high variability in the types of siderophores detected between the two cruises, with the exception of ferrioxamines. Differences in siderophore composition between the two cruises may reflect the fast turnover of siderophores, as previous incubation studies suggest that siderophore production can change on daily or weekly timescales (Mohamed and Gledhill 2017; Bundy et al. 2018). Considering the large compositional difference between the two cruises, it is interesting that the suite of ferrioxamines were identified from both cruises. It may be possible that the current siderophore analysis method preferentially extracts and isolates ferrioxamines, especially as ferrioxamines are ubiquitously detected from earlier studies (Boiteau et al. 2016, 2019; Bundy et al. 2018). It may be also possible that ferrioxamines are more commonly observed because they are more common siderophores that can be produced and used by a much wider variety of microbes than other siderophores.

Siderophore-related genes and transcripts

Our dissolved siderophore data provide information about which molecules exist in the water column at the time of our sampling. However, these snapshots of siderophore distributions alone do not reflect whether in situ microbial communities are capable of siderophore production and uptake. To gain further insight into the interactions between the dissolved siderophore pool and microbial activity, we used environmental metagenomes and metatranscriptomes to provide an overview of the genetic potential and expression levels of siderophore biosynthesis and uptake in surface communities across latitudes.

Siderophore biosynthesis and uptake potential were widely represented across the transects (Fig. 6a). This is consistent with the results of previous studies that found siderophore biosynthesis genes and Ton-B dependent outer membrane transporters of siderophores to be globally common in open ocean datasets (Tang et al. 2012; Garber et al. 2020). Both siderophore synthesis and uptake gene abundances significantly increased with latitude by approximately 1.5- and 3-fold across each cruise transect (Fig. 6a), whereas both siderophore synthesis and uptake transcript abundances also increased with latitude by approximately 8- and 5-fold across each cruise transect (Fig. 6b). Increasing abundances of siderophore related genes and transcripts may be partly driven by corresponding increases in heterotrophic bacterial abundances with latitude (by 1.9- and 2.7-fold across each cruise transect; Fig. 1h). Given the greater fold change in transcript abundances across latitude compared to gene abundances, siderophore synthesis and uptake may be more prominent in higher latitudes relative to lower latitudes. It is also interesting that siderophore synthesis and uptake transcript abundances in the SAFZ were higher than abundances in the NPTZ in 2017 (post hoc Tukey test, p = 0.08 and 0.03, respectively; Fig. 6b), whereas siderophore concentrations were lower in the SAFZ (Fig. 2b). This difference may be potentially due to a longer turnover time of the siderophore pool relative to that of the transcript pool. Specifically, dust input may have triggered rapid increases in transcription of siderophore biosynthesis genes in the NPTZ and high production of siderophores, but high siderophore concentrations may have subsequently relieved iron limitation in this area and led to reduced transcription of siderophore synthesis and uptake genes in this area.

PirA gene family was most frequently found in both metagenomes and metatranscriptomes among the siderophore transport gene families searched for (Supporting Information Figs. S3, S5). As PirA is a TonB-dependent receptor that was identified in *Pseudomonas aeruginosa* and *Acinetobacter baumannii* (Moynié et al. 2017), the abundance of PirA in both datasets may reflect the prevalence of TonB-dependent receptors, which are associated with uptake of iron-siderophore complexes (Moeck and Coulton 2002; Noinaj et al. 2010). VabA, VabE, and VabF families were the most commonly

detected among the siderophore synthesis gene families (Supporting Information Figs. S3, S5). vab genes were initially identified to mediate biosynthesis of vanchrobactin in *Vibrio anguillarum*, but these genes were also found to be highly homologous to multiple NRPS from other species (Balado et al. 2006). Therefore, the abundance of these gene families in our data do not necessarily suggest the ubiquity of vanchrobactin biosynthesis pathway in particular, but rather represent the presence of multiple NRPS siderophore biosynthesis pathways.

Microbial groups that harbor the majority of siderophore related genes were also actively transcribing those genes. Specifically, Gammaproteobacteria and Alphaproteobacteria were contributing most to gene and transcript abundances for both siderophore synthesis and uptake functions (Supporting Information Figs. S4, S6). High contribution of these two taxonomic groups to siderophore-related gene abundances is consistent with findings from a previous study which found that most siderophore transporters in the GOS metagenome dataset came from Gammaproteobacteria (63%) Alphaproteobacteria (31%; Tang et al. 2012). In comparison, a higher proportion of siderophore transport gene and transcript abundances were derived from the Bacteroidetes/ Chlorobi group relative to siderophore synthesis gene and transcript abundances (Supporting Information Figs. S4, S6). This may indicate that some members of this taxonomic group are capable of utilizing siderophores produced by other microbes rather than synthesizing siderophores on their own.

We further tried to directly connect transcription of individual iron-siderophore complex transporters to the specific compounds we identified in situ by using a stricter targeted analysis of the metatranscriptomes. In particular, we examined transcript abundances of ferrioxamine, amphibactin, and salmochelin transporter homologs as a means to detect active uptake of siderophores identified from our samples. Since siderophore receptors are closely related to other TonB-dependent receptors that transport other compounds such as hemes and cobalamins (Stojiljkovic and Hantke 1992), using custom-built HMM profiles with sequences of specific siderophore outer membrane transporter genes we are highly confident in (Supporting Information Fig. S1) makes this analysis highly conservative. Putative transporter homologs of these siderophores were predominantly transcribed by Gammaproteobacteria (Fig. 6c), in accordance with the metagenome analysis that indicated Gammaproteobacteria carried the majority of siderophore transport genes. Earlier studies also repeatedly found members of Gammaproteobacteria to possess a wide range of siderophore transporters relative to other bacterial groups (Hopkinson and Barbeau 2012; Tang et al. 2012; Debeljak et al. 2019). We expected to find amphibactin and ferrioxamine transporter genes to be transcribed by Gammaproteobacteria, as amphibactins and ferrioxamines are currently known to be produced by multiple gammaproteobacterial taxa, including Vibrio and Azotobacter, and Actinobacteria (Martinez et al. 2003; Wang et al. 2014; Zhang et al. 2019). Interestingly, we also detected

ferrioxamine-amphibactin-ferrichrome transporter homologs in Alphaproteobacteria reference genomes (Supporting Information Fig. S1) and detected expression of these homologs in the metatranscriptomes (Fig. 6c). No studies to date indicate ferrioxamine and amphibactins can be synthesized or utilized by taxa other than Gammaproteobacteria, in part because they have been the focus of laboratory studies (Hopkinson and Barbeau 2012). However, multiple Rhodobacterales species, including Rhodobacter, Roseovirus, Sulfitobacter, and Oceanicola, have genes to transport ferrichrome, a hydroxamate-type siderophore similar to ferrioxamine and amphibactin (Rodionov et al. 2006; Hider and Kong 2010). The high protein sequence similarity (28-55%) between ferrioxamine, amphibactin and ferrichrome transporters makes it difficult to distinguish them from one another. Thus, some of the transcripts recruited by our reference tree may be ferrichrome uptake transporters, rather than ferrioxamine or amphibactin transporters. Although we did not detect ferrichrome from seawater, it is possible that the ferrichrome pool has a rapid turnover and its concentration was too low to be detected. Additional studies are required to discern the specific function(s) of these transporter homologs.

Ferrioxamine and amphibactin transporter transcript inventories from Vibrionales were generally more abundant at northern stations (Fig. 6c; Supporting Information Fig. S7). Vibrionales are copiotrophic bacteria that are usually present in low abundance, but can quickly grow with additional nutrient pulses from bloom events (Westrich et al. 2016). Multiple species of Vibrio can produce and take up amphibactin, and at least one species of Vibrio is capable of exogenous ferrioxamine uptake (Gauglitz et al. 2021). Higher ferrioxamine and amphibactin transporter transcript abundances at higher latitudes by Vibrionales may reflect higher abundances of Vibrionales or increased induction of siderophore-mediated iron uptake pathways in this environment. Ferrioxamine and amphibactin transporter transcripts from Altermonadales in 2017 were also more abundant at 29.6°N relative to other latitudes (Fig. 6c). Ferrioxamine transporter transcripts may be produced by taxa such as Pseudoalteromonas and Alteromonas, which are able to assimilate ferrioxamine-bound iron (Armstrong et al. 2004). However, it is currently unclear whether high transcript abundance at 29.6°N was caused by significant differences in per cell transcript accumulation or a more abundant Altermonadales population as we cannot normalize the transcript abundances to microbial biomass.

While ferrioxamine and amphibactin transporter transcripts were produced by multiple Gammaproteobacterial and possibly Alphaproteobacterial taxa, transcript homologs of the salmochelin–enterobactin transporter were predominantly detected in the Gammaproteobacterial lineage Oceanospiralles. Salmochelin is a C-glycosylated derivative of enterobactin, and both salmochelin and enterobactin are known to be produced by the Enterobacterales, including *Escherichia coli*,

Salmonella, and Klebsiella (Hantke et al. 2003; Müller et al. 2009). Although iroN and fepA genes are often annotated as salmochelin and enterobactin transporter genes, respectively, both receptors can transport both siderophores (Watts et al. 2012), which makes it difficult to discern these transport functions from each other. Our observation that salmochelin-enterobactin transporter homologs are restricted primarily to Oceanospiralles, as well as the low abundance of associated transcripts, suggests that salmochelin or enterobactin may be utilized by a smaller subset of microbes than ferrioxamines or amphibactins. Given salmochelin and enterobactin uptake is limited to fewer microbes compared to ferrioxamine and amphibactin uptake, their production may also be low, considering the high metabolic cost of siderophore production. If so, this would result in much lower concentrations of salmochelin and enterobactin in the ocean than ferrioxamine and amphibactin, which may partly explain why we did not find enterobactin in this study (although we putatively identified salmochelin with low confidence based on m/z matching). Future characterization of salmochelin and enterobactin biosynthesis pathways may help us address this hypothesis by allowing the analysis of transcripts involved in salmochelin and enterobactin biosynthesis in the environment. Nevertheless, changes in the taxonomic composition of microbial groups that transcribe siderophore transporters suggest that several important bacterial taxa can compete for iron at different latitudes, perhaps contributing to niche differentiation in taxa that actively take up siderophore-bound iron.

Conclusions

The widespread presence of siderophores across a large range in latitude and depth in the North Pacific highlights the ubiquitous use of siderophores in oceanic iron cycling. Siderophores made up on average $2.4\% \pm 5.4\%$ (or 0–30%) of the total dissolved iron pool in our study sites. Within this pool, a wide variety of siderophores were identified, including ferrioxamines and amphibactins-the two most commonly identified siderophores in the ocean thus far-as well as putative photoreactive and fungal siderophores. Siderophore distribution patterns were not directly correlated to individual environmental parameters we measured during the two cruises, such as microbial biomass or dissolved iron, but were rather shaped by an interplay of microbial production and uptake. For instance, high siderophore concentrations and lower abundances of siderophore uptake transcripts abundances in the NPTZ in 2017 may reflect changes in the transcriptional response of the local microbial community to the dust deposition event. In addition, distinct microbial groups within Gammaproteobacteria and potentially Alphaproteobacteria were actively using ferrioxamine, amphibactin, and salmochelin in the surface ocean at different latitudes, which suggest that diverse microbial taxa are driving siderophore distributions.

Although our measurements represent a snapshot of siderophore concentrations at the time of our sampling, a time series of repeated dissolved siderophore profiles or intracellular siderophore secretion and uptake rate measurements may provide additional insight on the timescale of siderophore production, uptake and recycling by microbes, and will provide key insights into how microbes regulate iron availability in the open ocean.

Data availability statement

Temperature, salinity, nutrients, dissolved iron, POC, NCP, flow cytometry, and total siderophore concentrations are available at Simons CMAP (https://simonscmap.com/) and Zenodo (10.5281/zenodo.4104636 and 10.5281/zenodo.4079505). Raw mass spectrometry data files for siderophore analysis are deposited at MassIVE (https://massive.ucsd.edu/) and will be made public with publication. Sequence data for metagenomes and metatranscriptomes from Gradients 1 and 2 are available under BioProject PRJNA858011, PRJNA 492143, and PRJNA816919.

References

- Adly, C. L., J.-E. Tremblay, R. T. Powell, E. Armstrong, G. Peers, and N. M. Price. 2015. Response of heterotrophic bacteria in a mesoscale iron enrichment in the northeast subarctic Pacific Ocean: Bacterial response in an iron-enrichment. Limnol. Oceanogr. **60**: 136–148. doi:10.1002/lno.10013
- Armstrong, E., J. Granger, E. L. Mann, and N. M. Price. 2004. Outer-membrane siderophore receptors of heterotrophic oceanic bacteria. Limnol. Oceanogr. **49**: 579–587. doi:10. 4319/lo.2004.49.2.0579
- Årstøl, E., and M. F. Hohmann-Marriott. 2019. Cyanobacterial siderophores—Physiology, structure, biosynthesis, and applications. Mar. Drugs **17**: 281. doi:10.3390/md17050281
- Baakza, A., A. K. Vala, B. P. Dave, and H. C. Dube. 2004. A comparative study of siderophore production by fungi from marine and terrestrial habitats. J. Exp. Mar. Biol. Ecol. 311: 1–9. doi:10.1016/j.jembe.2003.12.028
- Baker, A. R., and P. L. Croot. 2010. Atmospheric and marine controls on aerosol iron solubility in seawater. Mar. Chem. **120**: 4–13. doi:10.1016/j.marchem.2008.09.003
- Balado, M., C. R. Osorio, and M. L. Lemos. 2006. A gene cluster involved in the biosynthesis of vanchrobactin, a chromosome-encoded siderophore produced by *Vibrio anguillarum*. Microbiology **152**: 3517–3528. doi:10.1099/mic.0.29298-0
- Barbeau, K., E. L. Rue, C. G. Trick, K. W. Bruland, and A. Butler. 2003. Photochemical reactivity of siderophores produced by marine heterotrophic bacteria and cyanobacteria based on characteristic Fe(III) binding groups. Limnol. Oceanogr. 48: 1069–1078. doi:10.4319/lo.2003.48.3.1069

- Boiteau, R. M., and others. 2016. Siderophore-based microbial adaptations to iron scarcity across the eastern Pacific Ocean. Proc. Natl. Acad. Sci. U.S.A. **113**: 242–14242. doi: 10.1073/pnas.1608594113
- Boiteau, R. M., C. P. Till, T. H. Coale, J. N. Fitzsimmons, K. W. Bruland, and D. J. Repeta. 2019. Patterns of iron and siderophore distributions across the California Current System. Limnol. Oceanogr. **64**: 376–389. doi:10.1002/lno.11046
- Bolger, A. M., M. Lohse, and B. Usadel. 2014. Trimmomatic: A flexible trimmer for Illumina sequence data. Bioinformatics **30**: 2114–2120. doi:10.1093/bioinformatics/btu170
- Boström, K. H., K. Simu, Å. Hagström, and L. Riemann. 2004. Optimization of DNA extraction for quantitative marine bacterioplankton community analysis: DNA extraction from bacterioplankton. Limnol. Oceanogr. Methods **2**: 365–373. doi:10.4319/lom.2004.2.365
- Bray, N. L., H. Pimentel, P. Melsted, and L. Pachter. 2016. Near-optimal probabilistic RNA-seq quantification. Nat. Biotechnol. **34**: 525–527. doi:10.1038/nbt.3519
- Buck, K. N., J. Moffett, K. A. Barbeau, R. M. Bundy, Y. Kondo, and J. Wu. 2012. The organic complexation of iron and copper: An intercomparison of competitive ligand exchange-adsorptive cathodic stripping voltammetry (CLE-ACSV) techniques: GEOTRACES speciation intercomparison. Limnol. Oceanogr. Methods 10: 496–515. doi:10.4319/lom.2012. 10.496
- Buck, K. N., P. N. Sedwick, B. Sohst, and C. A. Carlson. 2018. Organic complexation of iron in the eastern tropical South Pacific: Results from US GEOTRACES Eastern Pacific Zonal Transect (GEOTRACES cruise GP16). Mar. Chem. **201**: 229–241. doi:10.1016/j.marchem.2017.11.007
- Bundy, R. M., H. A. N. Abdulla, P. G. Hatcher, D. V. Biller, K. N. Buck, and K. A. Barbeau. 2015. Iron-binding ligands and humic substances in the San Francisco Bay estuary and estuarine-influenced shelf regions of coastal California. Mar. Chem. **173**: 183–194. doi:10.1016/j.marchem.2014. 11.005
- Bundy, R. M., R. M. Boiteau, C. McLean, K. A. Turk-Kubo, M. R. McIlvin, M. A. Saito, B. A. S. Van Mooy, and D. J. Repeta. 2018. Distinct siderophores contribute to iron cycling in the mesopelagic at station ALOHA. Front. Mar. Sci. 5: 61. doi:10.3389/fmars.2018.00061
- Capella-Gutierrez, S., J. M. Silla-Martinez, and T. Gabaldon. 2009. trimAl: A tool for automated alignment trimming in large-scale phylogenetic analyses. Bioinformatics **25**: 1972–1973. doi:10.1093/bioinformatics/btp348
- Carrano, C. J., M. Jordan, H. Drechsel, and D. G. Schmid. 2001. Heterobactins: A new class of siderophores from *Rhodococcus erythropolis* IGTS8 containing both hydroxamate and catecholate donor groups. Biometals **14**: 119–125.
- Carroll, C. S., and M. M. Moore. 2018. Ironing out siderophore biosynthesis: A review of non-ribosomal peptide synthetase (NRPS)-independent siderophore synthetases. Crit. Rev.

- Biochem. Mol. Biol. **53**: 356–381. doi:10.1080/10409238. 2018.1476449
- Coesel, S. N., B. P. Durham, R. D. Groussman, S. K. Hu, D. A. Caron, R. L. Morales, F. Ribalet, and E. V. Armbrust. 2021. Diel transcriptional oscillations of light-sensitive regulatory elements in open-ocean eukaryotic plankton communities. Proc. Natl. Acad. Sci. U.S.A. **118**: e2011038118. doi:10. 1073/pnas.2011038118
- Darriba, D., G. L. Taboada, R. Doallo, and D. Posada. 2011. ProtTest 3: Fast selection of best-fit models of protein evolution. Bioinformatics **27**: 1164–1165. doi:10.1093/bioinformatics/btr088
- Debeljak, P., E. Toulza, S. Beier, S. Blain, and I. Obernosterer. 2019. Microbial iron metabolism as revealed by gene expression profiles in contrasted Southern Ocean regimes. Environ. Microbiol. **21**: 2360–2374. doi:10.1111/1462-2920.14621
- Djoumbou-Feunang, Y., and others. 2019. CFM-ID 3.0: Significantly improved ESI-MS/MS prediction and compound identification. Metabolites **9**: 72. doi:10.3390/metabo9040072
- Durham, B. P., and others. 2019. Sulfonate-based networks between eukaryotic phytoplankton and heterotrophic bacteria in the surface ocean. Nat. Microbiol. **4**: 1706–1715. doi:10.1038/s41564-019-0507-5
- Eddy, S. R. 2011. Accelerated profile HMM searches. PLoS Comput. Biol. **7**: e1002195. doi:10.1371/journal.pcbi. 1002195
- Edgar, R. C. 2010. Search and clustering orders of magnitude faster than BLAST. Bioinformatics **26**: 2460–2461. doi:10. 1093/bioinformatics/btq461
- Follett, C. L., S. Dutkiewicz, G. Forget, B. B. Cael, and M. J. Follows. 2021. Moving ecological and biogeochemical transitions across the North Pacific. Limnol. Oceanogr. **66**: 2442–2454. doi:10.1002/lno.11763
- Garber, A. I., K. H. Nealson, A. Okamoto, S. M. McAllister, C. S. Chan, R. A. Barco, and N. Merino. 2020. FeGenie: A comprehensive tool for the identification of iron genes and iron gene neighborhoods in genome and metagenome assemblies. Front. Microbiol. 11: 37. doi:10.3389/fmicb. 2020.00037
- Gauglitz, J. M., R. M. Boiteau, C. McLean, L. Babcock-Adams, M. R. McIlvin, D. M. Moran, D. J. Repeta, and M. A. Saito. 2021. Dynamic proteome response of a marine vibrio to a gradient of iron and ferrioxamine bioavailability. Mar. Chem. **229**: 103913. doi:10.1016/j.marchem.2020.103913
- Gledhill, M., and C. M. G. van den Berg. 1994. Determination of complexation of iron(III) with natural organic complexing ligands in seawater using cathodic stripping voltammetry. Mar. Chem. **47**: 41–54. doi:10.1016/0304-4203(94)90012-4
- Gledhill, M., and K. N. Buck. 2012. The organic complexation of iron in the marine environment: A review. Front. Microbiol. **3**: 69. doi:10.3389/fmicb.2012.00069

- Grabherr, M. G., and others. 2011. Full-length transcriptome assembly from RNA-seq data without a reference genome. Nat. Biotechnol. **29**: 644–652. doi:10. 1038/nbt.1883
- Gradoville, M. R., and others. 2020. Latitudinal constraints on the abundance and activity of the cyanobacterium UCYN-A and other marine diazotrophs in the North Pacific. Limnol. Oceanogr. **65**: 1858–1875. doi:10.1002/lno.11423
- Gulick, A. M. 2017. Nonribosomal peptide synthetase biosynthetic clusters of ESKAPE pathogens. Nat. Prod. Rep. **34**: 981–1009. doi:10.1039/C7NP00029D
- Hantke, K., G. Nicholson, W. Rabsch, and G. Winkelmann. 2003. Salmochelins, siderophores of *Salmonella enterica* and uropathogenic *Escherichia coli* strains, are recognized by the outer membrane receptor IroN. Proc. Natl. Acad. Sci. U.S.A. **100**: 3677–3682. doi:10.1073/pnas.0737682100
- Hassler, C. S., V. Schoemann, M. Boye, A. Tagliabue, M. Rozmarynowycz, and R. M. L. McKay. 2012. Iron bioavailability in the Southern Ocean. Oceanogr. Mar. Biol. Annu. Rev. **50**: 1–64.
- Hider, R. C., and X. Kong. 2010. Chemistry and biology of siderophores. Nat. Prod. Rep. **27**: 637. doi:10.1039/b906679a
- Hogle, S. L. 2019. MARMICRODB database for taxonomic classification of (marine) metagenomes (1.00) [Data set]. doi: 10.5281/zenodo.3520509
- Holinsworth, B., and J. D. Martin. 2009. Siderophore production by marine-derived fungi. Biometals **22**: 625–632. doi: 10.1007/s10534-009-9239-y
- Hopkinson, B. M., and K. A. Barbeau. 2012. Iron transporters in marine prokaryotic genomes and metagenomes: Iron transporters in marine prokaryotes. Environ. Microbiol. **14**: 114–128. doi:10.1111/j.1462-2920.2011.02539.x
- Hunter, K. A., and P. W. Boyd. 2007. Iron-binding ligands and their role in the ocean biogeochemistry of iron. Environ. Chem. **4**: 221. doi:10.1071/EN07012
- Johnson, K. S., R. M. Gordon, and K. H. Coale. 1997. What controls dissolved iron concentrations in the world ocean? Mar. Chem. **57**: 137–161. doi:10.1016/S0304-4203(97) 00043-1
- Juranek, L. W., and others. 2020. The importance of the phytoplankton "middle class" to ocean net community production. Global Biogeochem. Cycl. **34**: 12. doi:10.1029/2020GB006702
- Katoh, K., and D. M. Standley. 2013. MAFFT multiple sequence alignment software version 7: Improvements in performance and usability. Mol. Biol. Evol. **30**: 772–780. doi:10.1093/molbev/mst010
- Keeling, P. J., and others. 2014. The Marine Microbial Eukaryote Transcriptome Sequencing Project (MMETSP): Illuminating the functional diversity of eukaryotic life in the oceans through transcriptome sequencing. PLoS Biol. **12**: e1001889. doi:10.1371/journal.pbio.1001889
- Kem, M. P., H. K. Zane, S. D. Springer, J. M. Gauglitz, and A. Butler. 2014. Amphiphilic siderophore production by oil-

- associating microbes. Metallomics **6**: 1150–1155. doi:10. 1039/C4MT00047A
- Kraemer, S. M., A. Butler, P. Borer, and J. Cervini-Silva. 2005. Siderophores and the dissolution of iron-bearing minerals in marine systems. Rev. Mineral. Geochem. **59**: 53–84. doi: 10.2138/rmg.2005.59.4
- Kramer, J., Ö. Özkaya, and R. Kümmerli. 2020. Bacterial siderophores in community and host interactions. Nat. Rev. Microbiol. **18**: 152–163. doi:10.1038/s41579-019-0284-4
- Krewulak, K. D., and H. J. Vogel. 2008. Structural biology of bacterial iron uptake. Biochim. Biophys. Acta Biomembr. **1778**: 1781–1804. doi:10.1016/j.bbamem.2007.07.026
- Kügler, S., R. E. Cooper, J. Boessneck, K. Küsel, and T. Wichard. 2020. Rhizobactin B is the preferred siderophore by a novel *Pseudomonas* isolate to obtain iron from dissolved organic matter in peatlands. Biometals **33**: 415–433. doi:10.1007/s10534-020-00258-w
- Lagerström, M. E., M. P. Field, M. Séguret, L. Fischer, S. Hann, and R. M. Sherrell. 2013. Automated on-line flow-injection ICP-MS determination of trace metals (Mn, Fe, Co, Ni, Cu and Zn) in open ocean seawater: Application to the GEOTRACES program. Mar. Chem. **155**: 71–80. doi:10. 1016/j.marchem.2013.06.001
- Magoc, T., and S. L. Salzberg. 2011. FLASH: Fast length adjustment of short reads to improve genome assemblies. Bioinformatics **27**: 2957–2963. doi:10.1093/bioinformatics/btr507
- Marie, D., F. Partensky, D. Vaulot, and C. Brussaard. 1999. Enumeration of phytoplankton, bacteria, and viruses in marine samples. Curr. Protoc. Cytom. **10**: 11–11. doi:10. 1002/0471142956.cy1111s10
- Martinez, J. S., J. N. Carter-Franklin, E. L. Mann, J. D. Martin, M. G. Haygood, and A. Butler. 2003. Structure and membrane affinity of a suite of amphiphilic siderophores produced by a marine bacterium. Proc. Natl. Acad. Sci. U.S.A. **100**: 3754–3759. doi:10.1073/pnas.0637444100
- Matsen, F. A., R. B. Kodner, and E. V. Armbrust. 2010. pplacer: Linear time maximum-likelihood and Bayesian phylogenetic placement of sequences onto a fixed reference tree. BMC Bioinform. **11**: 538. doi:10.1186/1471-2105-11-538
- Mawji, E., and others. 2008. Hydroxamate siderophores: Occurrence and importance in the Atlantic Ocean. Environ. Sci. Technol. **42**: 8675–8680. doi:10.1021/es801884r
- Menzel, P., K. L. Ng, and A. Krogh. 2016. Fast and sensitive taxonomic classification for metagenomics with Kaiju. Nat. Commun. **7**: 11257. doi:10.1038/ncomms11257
- Moeck, G. S., and J. W. Coulton. 2002. TonB-dependent iron acquisition: Mechanisms of siderophore-mediated active transport: TonB-dependent iron acquisition. Mol. Microbiol. **28**: 675–681. doi:10.1046/j.1365-2958.1998. 00817.x
- Mohamed, K. N., and M. Gledhill. 2017. Identification and quantification of siderophore type chelators in the incubation samples. J. Res. Anal. **3**: 96–107.

- Moore, C. M., and s. 2013. Processes and patterns of oceanic nutrient limitation. Nat. Geosci. **6**: 701–710. doi:10.1038/ngeo1765
- Moynié, L., and others. 2017. Structure and function of the PiuA and PirA siderophore-drug receptors from *Pseudomonas aeruginosa* and *Acinetobacter baumannii*. Antimicrob. Agents Chemother. **61**: e02531-16. doi:10.1128/AAC.02531-16
- Müller, S. I., M. Valdebenito, and K. Hantke. 2009. Salmochelin, the long-overlooked catecholate siderophore of *Salmonella*. Biometals **22**: 691–695. doi:10.1007/s10534-009-9217-4
- Neilands, J. B. 1981. Microbial iron compounds. Annu. Rev. Biochem. **50**: 715–731. doi:10.1146/annurev.bi.50.070181. 003435
- Noinaj, N., M. Guillier, T. J. Barnard, and S. K. Buchanan. 2010. TonB-dependent transporters: Regulation, structure, and function. Annu. Rev. Microbiol. **64**: 43–60. doi:10. 1146/annurev.micro.112408.134247
- Parrello, D., A. Zegeye, C. Mustin, and P. Billard. 2016. Side-rophore-mediated iron dissolution from nontronites is controlled by mineral cristallochemistry. Front. Microbiol. **7**: 423. doi:10.3389/fmicb.2016.00423
- Pinedo-González, P., and others. 2020. Anthropogenic Asian aerosols provide Fe to the North Pacific Ocean. Proc. Natl. Acad. Sci. U.S.A. **117**: 27862–27868. doi:10.1073/pnas. 2010315117
- Polovina, J. J., E. Howell, D. R. Kobayashi, and M. P. Seki. 2001. The transition zone chlorophyll front, a dynamic global feature defining migration and forage habitat for marine resources. Prog. Oceanogr. **49**: 469–483. doi:10. 1016/S0079-6611(01)00036-2
- Rice, P., I. Longden, and A. Bleasby. 2000. EMBOSS: The European Molecular Biology Open Software Suite. Trends Genet. **16**: 276–277.
- Roden, G. 1991. Subarctic–subtropical transition zone of the North Pacific large scale aspects and mesoscale structure. NOAA technical report 105. NOAA.
- Rodionov, D. A., M. S. Gelfand, J. D. Todd, A. R. J. Curson, and A. W. B. Johnston. 2006. Computational reconstruction of iron- and manganese-responsive transcriptional networks in α -proteobacteria. PLoS Comput. Biol. **2**: 1568–1585.
- Ruttkies, C., E. L. Schymanski, S. Wolf, J. Hollender, and S. Neumann. 2016. MetFrag relaunched: Incorporating strategies beyond in silico fragmentation. J. Cheminform. 8: 3. doi:10.1186/s13321-016-0115-9
- Sandy, M., and A. Butler. 2009. Microbial iron acquisition: Marine and terrestrial siderophores. Chem. Rev. **109**: 4580–4595. doi:10.1021/cr9002787
- Satinsky, B. M., S. M. Gifford, B. C. Crump, and M. A. Moran. 2013. Use of internal standards for quantitative metatranscriptome and metagenome analysis, p. 237–250. *In* Methods in enzymology. Elsevier.

- Shaked, Y., K. N. Buck, T. Mellett, and M. T. Maldonado. 2020. Insights into the bioavailability of oceanic dissolved Fe from phytoplankton uptake kinetics. ISME J. **14**: 1182–1193. doi:10.1038/s41396-020-0597-3
- Stamatakis, A. 2014. RAxML version 8: A tool for phylogenetic analysis and post-analysis of large phylogenies. Bioinformatics **30**: 1312–1313. doi:10.1093/bioinformatics/btu033
- Steinegger, M., and J. Söding. 2018. Clustering huge protein sequence sets in linear time. Nat. Commun. **9**: 2542. doi: 10.1038/s41467-018-04964-5
- Stojiljkovic, I., and K. Hantke. 1992. Hemin uptake system of Yersinia enterocolitica: Similarities with other TonB-dependent systems in gram-negative bacteria. EMBO J. **11**: 4359–4367. doi:10.1002/j.1460-2075.1992.tb05535.x
- Sumner, L. W., and others. 2007. Proposed minimum reporting standards for chemical analysis: Chemical Analysis Working Group (CAWG) Metabolomics Standards Initiative (MSI). Metabolomics **3**: 211–221. doi:10.1007/s11306-007-0082-2
- Tagliabue, A., A. R. Bowie, P. W. Boyd, K. N. Buck, K. S. Johnson, and M. A. Saito. 2017. The integral role of iron in ocean biogeochemistry. Nature 543: 51–59. doi:10.1038/nature21058
- Tang, K., N. Jiao, K. Liu, Y. Zhang, and S. Li. 2012. Distribution and functions of TonB-dependent transporters in marine bacteria and environments: Implications for dissolved organic matter utilization. PLoS One **7**: e41204. doi: 10.1371/journal.pone.0041204
- Toulza, E., A. Tagliabue, S. Blain, and G. Piganeau. 2012. Analysis of the Global Ocean sampling (GOS) project for trends in iron uptake by surface ocean microbes. PLoS One **7**: e30931. doi:10.1371/journal.pone.0030931
- Vink, S., E. A. Boyle, C. I. Measures, and J. Yuan. 2000. Automated high resolution determination of the trace elements iron and aluminium in the surface ocean using a towed fish coupled to flow injection analysis. Deep Sea Res. I Oceanogr. Res. Pap. **16**: 1141–1156. doi:10.1016/S0967-0637(99)00074-6
- Vraspir, J. M., and A. Butler. 2009. Chemistry of marine ligands and siderophores. Annu. Rev. Mar. Sci. 1: 43–63. doi:10.1146/annurev.marine.010908.163712
- Wagener, T., E. Pulido-Villena, and C. Guieu. 2008. Dust iron dissolution in seawater: Results from a one-year time-series

- in the Mediterranean Sea. Geophys. Res. Lett. **35**: L16601. doi:10.1029/2008GL034581
- Wang, W., Z. Qiu, H. Tan, and L. Cao. 2014. Siderophore production by actinobacteria. Biometals **27**: 623–631. doi:10. 1007/s10534-014-9739-2
- Watts, R. E., M. Totsika, V. L. Challinor, A. N. Mabbett, G. C. Ulett, J. J. D. Voss, and M. A. Schembri. 2012. Contribution of siderophore systems to growth and urinary tract colonization of asymptomatic bacteriuria *Escherichia coli*. Infect. Immun. **80**: 333–344. doi:10.1128/IAI.05594-11
- Westrich, J. R., A. M. Ebling, W. M. Landing, J. L. Joyner, K. M. Kemp, D. W. Griffin, and E. K. Lipp. 2016. Saharan dust nutrients promote *Vibrio* bloom formation in marine surface waters. Proc. Natl. Acad. Sci. U.S.A. **113**: 5964–5969. doi:10.1073/pnas.1518080113
- Zhang, X., O. Baars, and F. M. M. Morel. 2019. Genetic, structural, and functional diversity of low and high-affinity siderophores in strains of nitrogen fixing *Azotobacter chroococcum*. Metallomics **11**: 201–212. doi:10.1039/C8MT00236C

Acknowledgments

This work was supported by the Simons Foundation (426570 to R.M.B., S.G.J., E.V.A., D.L., L.J., A.E.I., and R.M.B.; 823165 to B.P.D.). The authors thank the SCOPE-Gradients team for assisting with sample collection, sharing data, and providing helpful feedback that improved this work. The authors thank L. Carlson and K. Heal for help with data acquisition on the Orbitrap; T. Ugrai for technical support on the ICP-MS; L. Pnueli and M. Peleg for their contributions to metagenome sample processing and sequence analysis; S. Curless and R. Foreman for nutrient analysis; J. McMillan, K. Cain, and A. Hynes for helping collecting and processing flow cytometry samples; D. Karl and A. White for constructive comments on the manuscript; and the captain and crew of the R/V *Marcus G. Langseth* and R/V *Ka'imikai-O-Kanaloa*.

Conflict of Interest

All authors declare that they have no conflicts of interest.

Submitted 02 March 2022 Revised 02 February 2023 Accepted 30 April 2023

Associate editor: Vanessa Hatje